Biomaterials Science

ROYAL SOCIETY OF CHEMISTRY

PAPER

View Article Online
View Journal | View Issue

Cite this: *Biomater. Sci.*, 2023, **11**, 7568

A transdermal drug delivery system based on dissolving microneedles for boron neutron capture therapy of melanoma†

Jiaxin Li,‡[a] Xueyi Wang,*‡[b,c] Zhaoshuo Wang,[d] Yu Zhao,[a] Ziyang Zhang,[a] Lanya Li,[b,c] Dandan Ding,[b,c] Junshu Guo,[b,c] Jinchao Zhang,[a] Huifang Liu *[a] and Zhenhua Li *[b,c]

Boron neutron capture therapy (BNCT) is a promising therapy for malignant tumors that requires selective and high concentrations of ^{10}B accumulation in tumor cells. Despite ongoing developments in novel boron agents and delivery carriers, the progress and clinical application of BNCT is still restricted by the low ^{10}B accumulation and tumor-to-normal tissue (T/N) ratio. Herein, a dissolving microneedle-based transdermal drug delivery system was specifically designed for BNCT in a mouse model of melanoma. By incorporating fructose-BPA (F-BPA) into PVA microneedle tips, this system successfully delivered sufficient F-BPA into the melanoma site after the application of only two patches. Notably, the T/N ratio achieved through the treatment combining PVA/F-BPA MNs with BNCT (PVA/F-BPA MNs-BNCT) surpassed 93.16, signifying a great improvement. Furthermore, this treatment approach effectively inhibited tumor growth and significantly enhanced the survival rate of the mice. In brief, our study introduces a novel, simple, and efficient administration strategy for BNCT, opening new possibilities for the design of nanomedicine for BNCT.

Received 1st August 2023,
Accepted 1st October 2023

DOI: 10.1039/d3bm01262j

rsc.li/biomaterials-science

1. Introduction

BNCT is a novel radiotherapy technique that has shown excellent inhibition of locally aggressive tumors.[1] The alpha particles and recoiling lithium-7 nuclei generated during the boron neutron capture reaction can cause DNA damage without affecting the surrounding healthy cells, due to their limited travelling distance, typically just tens of micrometers.[2] With this excellent advantage, BNCT is regarded as promising tumor-precise treatment to alleviate the suffering of cancer patients in current clinical treatment.

Currently, the preferred and most effective boron drug in clinical BNCT is L-*p*-boronophenylalanine (BPA).[3,4] With a chemical structure similar to tyrosine, BPA is targeted to access tumor cells mediated by the overexpressed L-amino acid transporter-1 (LAT-1).[5,6] However, its further clinical application is hampered by poor water solubility due to the neutral charge at physiological pH and the hydrophobic structure of phenylalanine. To address this problem, Yoshino *et al.* developed fructose-BPA (F-BPA) *via* covalent bonding between fructose and boronic acids in BPA, thereby increasing its water solubility.[7] Consequently, fructose-BPA has become the first choice in recent clinical studies.

Successful BNCT relies on several critical factors such as a sufficient concentration of accumulated ^{10}B (>20 μg ^{10}B per g tumor tissue) in tumor cells and a high distribution ratio of boron drug in tumor cells to normal cells (T/N >3 : 1).[4,8] An enhanced ^{10}B concentration within tumor cells and an optimal T/N ratio hold the key to achieving highly effective treatment, minimizing undesirable side effects and reducing patient discomfort. Regrettably, the therapeutic potential of BPA is sometimes hindered as it struggles to maintain its desired concentration within the cells owing to the efflux of intracellular BPA *via* LAT-1.[9] Therefore, in clinical treatment, fructose-BPA is transfused to patients throughout the irradiation process to maintain a high boron concentration in tumors. However, this

[a]*College of Pharmaceutical Science, Key Laboratory of Pharmaceutical Quality Control of Hebei Province, Hebei University, Baoding, 071002, China. E-mail: liu-huifang@163.com*
[b]*The 10th Affiliated Hospital of Southern Medical University (Dongguan People's Hospital), Dongguan, 523059, China. E-mail: zhenhuali@hbu.edu.cn, ixueyi@smu.edu.cn*
[c]*Guangdong Provincial Key Laboratory of Cardiac Function and Microcirculation, 510280 Guangzhou, China*
[d]*College of Chemistry & Environmental Science, Key Laboratory of Medicinal Chemistry and Molecular Diagnosis of Ministry of Education, Chemical Biology Key Laboratory of Hebei Province, Hebei University, Baoding, 071002, China*
†Electronic supplementary information (ESI) available. See DOI: **https://doi.org/10.1039/d3bm01262j**
‡These authors contributed equally to this work.

approach introduces complexity and uncertainty to treatment. Additionally, the T/N ratio of fructose-BPA is hard to exceed 4 : 1 *via* intravenous injection.[4,10] Thus, many novel boron drugs and delivery carriers, such as polymers,[5,6] ^{10}B carbon dots,[11] nanoparticles,[12–15] polymersomes,[16] and boronsomes,[17] have been developed for intravenous injection in BNCT. However, the traditional intravenous injection shows problems of insufficient drug accumulation in tumor tissue and drug distribution in multiple organs, giving rise to potential concerns regarding systemic toxicity. Hence, exploring new modes of administration to improve the ^{10}B concentration in tumor cells and the T/N ratio while also bringing simplicity and convenience to BNCT should be a key focus for optimizing clinical studies. Microneedles (MNs), composed of a patch with arrays of micron-sized needles, can effectively deliver drugs,[18] proteins,[19,20] genes,[21] vaccines,[22] antibodies,[23] microbes[24] and nanoparticles[25,26] to a targeted site *via* the transdermal route of administration. Therefore, a microneedle-based delivery system is a painless, non-invasive, and patient-compliant treatment and is expected to enhance local accumulation.[27,28] The microneedle-based delivery system has been successfully used to treat breast cancer,[29–31] skin carcinoma,[32,33] and glioma.[18,33,34]

Inspired by this, in the work, we developed a novel transdermal drug delivery system based on dissolving microneedles for enhanced BNCT. In detail, we designed PVA/F-BPA dissolving microneedles for BNCT of melanoma, with F-BPA loaded in the PVA tips (Fig. 1). Owing to the elevated concentration of the ^{10}B drug encapsulated within the microneedle tips, there was a notable augmentation in the accumulation of the drug within the targeted tumor site. Consequently, a substantial and reliable supply of the ^{10}B drug was ensured throughout the thermal neutron irradiation phase, ensuring the efficacy of BNCT. Moreover, the PVA/F-BPA microneedles demonstrated impressive proficiency in skin penetration, coupled with an outstanding dissolution capacity, leading to their complete disappearance within a mere five minutes post-penetration. Moreover, the intracellular uptake of ^{10}B was up to 21.7 ng per 10^6 cells after 3 h incubation even at a very low ^{10}B concentration of 3 ppm with PVA/F-BPA, which exceeded the critical concentration of ^{10}B for successful BNCT (16.67 ng per 10^6 cells).[4] For *in vivo* studies, neutron irradiation could significantly reduce the viability of B16-F10 cells incubated with F-BPA by directly killing B16-F10 cells and damaging DNA double-strand breaks to inhibit cell proliferation. Furthermore, in animal experiments, after treatment with two patches of PVA/F-BPA MNs on the subcutaneous melanoma, ^{10}B was taken up by 23.12 μg per g tumor tissue, showing a high uptake rate. In addition, the T/N ratio, the most critical factor in BNCT, was higher than 93.16, which was far superior to that obtained *via* administration using the intravenous injection method (the T/N ratio was 1–4 for intravenous injection in pre-

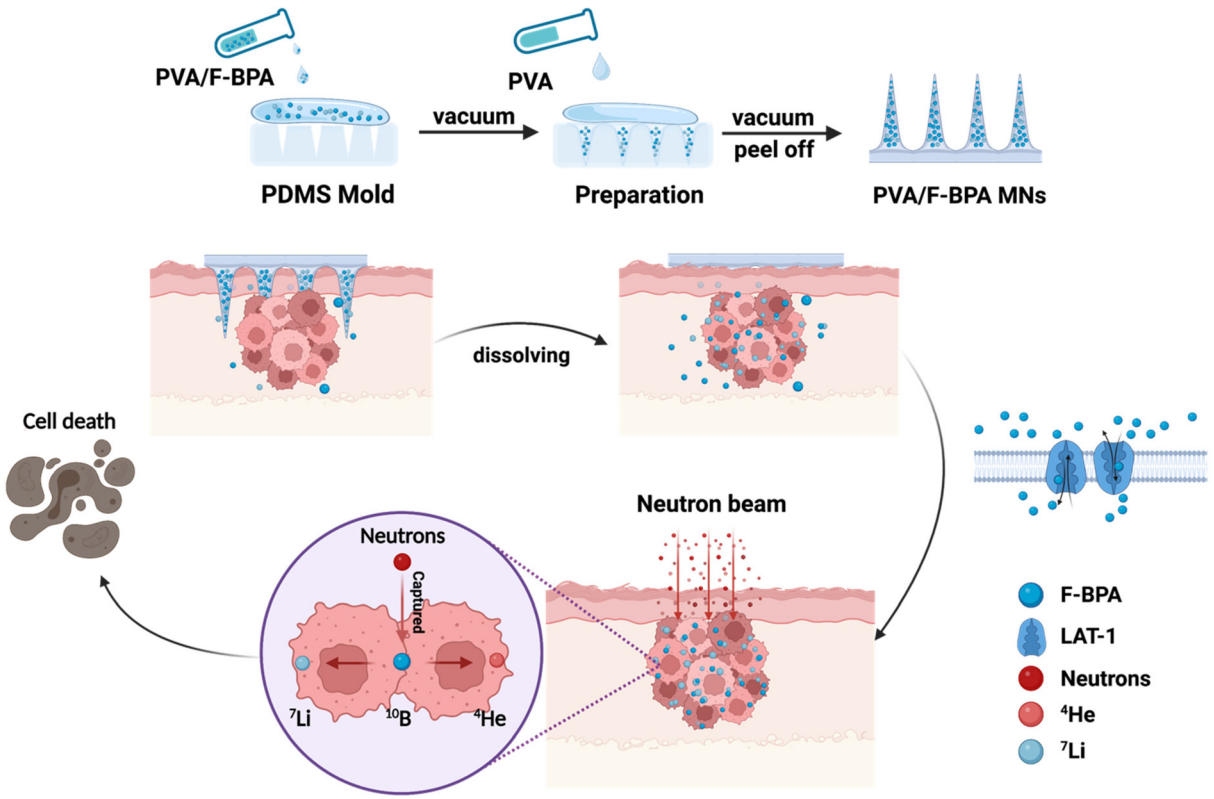

Fig. 1 Schematic illustration of the synthesis of facile fast-dissolving PVA/F-BPA MNs and their application in the BNCT treatment of melanoma. The figure was created with BioRender.com.

viously reported literature studies).[4–6,9,10,15,17] After neutron irradiation, tumor growth in microneedle-treated mice was significantly suppressed compared to other control groups. Therefore, a new treatment method with high efficiency, convenience and minimal damage to normal tissues is provided by our PVA/F-BPA MNs for BNCT treatment.

2. Materials and methods

2.1. Materials

^{10}BPA was purchased from HEC Pharmaceutical. PVA (M_w = 14 kDa) was purchased from EngineeringForLife. Fructose was purchased from China National Medicines Corporation Ltd. DAPI was purchased from Solarbio. γ-H2AX was purchased from Proteintech. Paraformaldehyde and D_2O were purchased from InnoChem. Crystal violet was purchased from Servicebio. HNO_3 was purchased from Damao. Cy5-fructose was purchased from Ruixi. A microneedle mold was purchased from Micropoint Technologies Pte Ltd. All BNCT experiments were carried out on BNCT devices at the China Spallation Neutron Source (CSNS), Dongguan.

2.2. Cells and animals

The culture medium of B16-F10 cells was RPMI-1640 with 10% fetal bovine serum and 1% penicillin–streptomycin. B16-F10 cells were cultured in a 37 °C humid environment containing 5% CO_2. All animal experiments were carried out following the requirements of the Laboratory Animal Ethics Committee of Hebei University and approved by the Laboratory Animal Ethics Committee of Southern Medical University.

2.3. Synthesis of fructose-BPA

BPA and fructose (at a molar ratio of 1 : 1.2) were added into water with stirring. Then 1 M NaOH solution was added dropwise into the mixture solution until the turbid solution turned clear. After 4 h, 1 M HCl solution was added dropwise into the reaction mixture to adjust the pH to 7.4. Then the solution was filtered using 0.22 μm PES syringe filters. Fructose-BPA was obtained as a white powder after freeze-drying and then characterized by ^{1}H NMR.

2.4. Preparation of microneedles

PVA microneedles: 0.25 g (M_w = 14 kDa) polyvinyl alcohol (PVA) was added to 1 mL ultra-pure water and stirred at 60 °C until it was completely dissolved. Then, 500 μL of ultrapure water was added to the mold groove at 30 °C under vacuum (−0.07 MPa) negative pressure. After repeated vacuuming 2–3 times, the excess liquid was removed. Then, the PDMS microneedle mold was filled with PVA solution and dried in a drying oven at 30 °C for 12 h to obtain a PVA microneedle array. The morphology of microneedles was characterized by SEM and a stereomicroscope.

PVA/F-BPA MNs: 200 mg of fructose-BPA was mixed with 250 mg mL^{-1} PVA solution and stirred well to form a mixture solution. The PVA/F-BPA MNs were obtained according to the preparation method of PVA microneedles.

2.5. Drug loading assay for PVA/F-BPA MNs

PVA/F-BPA MN tips (n = 5) were cut off with a surgical blade and placed in an Eppendorf tube with 68 wt% HNO_3, heated at 70 °C for 12 h. The liquid was filtered through 0.22 μm PES syringe filters and the ^{10}B content of the tips was determined by ICP-OES.

2.6. *In vitro* skin puncture test and H&E staining

The skin of isolated mice was punctured with microneedle pressure for 10 s. Then the PVA microneedle was removed and the area of microneedle action was applied with 1% Taipan blue solution for 20 min. The skin surface was wiped clean with cotton swabs and a stereomicroscope was used to observe whether a blue dot matrix was obtained. After the puncture test, the skin of mice was fixed with paraformaldehyde solution, and then paraffin-embedding and hematoxylin–eosin (H&E) staining were performed.

2.7. Mechanical strength test of PVA/F-BPA MNs

The mechanical strength of PVA/F-BPA MNs was measured using a rheometer. The tips of the microneedles were placed upward in the center of the horizontal load table at a speed of 2.0 μm s^{-1}, and the relationship between the load and the displacement of the microneedle was recorded.

2.8. Dissolution characteristics of PVA/F-BPA MNs

3% (w/v) agarose powder was dissolved in ultrapure water and boiled for 30 s. Then the solution was poured into a 6-well plate to cool and solidify, forming an agarose gel to simulate skin. PVA/F-BPA MNs were inserted into the agarose gel by pressure, and the microneedles were clamped after the indicated time to observe the dissolution of the needle tips.

2.9. Cellular uptake of F-BPA

B16-F10 cells (cell density: 1×10^6) were cultured in six-well plates for 24 h, and then fresh medium containing PVA/F-BPA solution was added and incubated for 3 hours. After washing with PBS 4–5 times, the collected cells were digested with HNO_3 and the ^{10}B content was measured by ICP-OES.

2.10. CCK-8 assay

B16-F10 cells were seeded at a density of 1×10^3 cells per well in a 96-well plate and pre-cultured for 24 hours. After each group of materials and cells were incubated for 3 h (irradiated or not irradiated with neutrons), fresh medium was replaced and incubation was continued for 18 h before 10 μL of CCK-8 solution was added to each well. The absorbance at 450 nm was measured by enzyme standardization and the data results were statistically analyzed with the PBS group. The calculation formula is as follows:

$$\text{Cell survival rate} = [(\text{As} - \text{Ab})/(\text{Ac} - \text{Ab})] \times 100\%$$

$$\text{Inhibition rate} = [(Ac - As)/(Ac - Ab)] \times 100\%$$

2.11. Cell cloning experiment

1×10^5 cells were laid in a 12-well plate and incubated overnight. The materials were incubated with cells for 3 h, and the cells were collected and subjected to neutron irradiation for 60 min (epithermal neutron flux: 3.37×10^7 n cm^{-2} s^{-1}, China Spallation Neutron Source, Dongguan). 200 cells were placed in a 6-well plate and cultured for 5 days. Then the cells were fixed with paraformaldehyde for 30 min and washed with PBS 3 times. After that, the cells were stained with crystal violet and washed slowly with ultra-pure water. The distribution of cell communities was observed using photographs, and colony formation was analyzed and counted using Image J.

The cell-stained crystal violet was dissolved in 1 mL of 10% acetic acid and collected. Then 100 μL of crystal violet solution from each group was put into a 96-well plate, and the absorbance was recorded at 570 nm using an enzyme labelling instrument to observe the cell growth of different groups.

2.12. DNA damage test

After the neutron irradiation of B16-F10 cells introduced above, 3×10^4 cells were transferred from a 0.6 mL EP tube to a confocal dish and incubated for 8 h. After the incubation, the liquid in the dish was aspirated and washed 3 times with PBS. Then 4% paraformaldehyde was added to fix the cells for 20 min and the cells were washed 3 times with PBS at 4 °C. After that, 500 μL of diluted Triton (0.5%) was added and then the cells were punctured for 20 min and washed 3–4 times with PBS at 4 °C, 1–2 min each time. Then the cells were blocked with 1% serum at 37 °C for 30 minutes, washed again with PBS 3 times at 4 °C, and then incubated with the γ-H2AX antibody (1 : 100) at 4 °C for 40 minutes. After washing 3 times with PBS, DAPI was added and incubated for another 8 minutes. Finally, 700 μL of PBS was added and the cells were observed using a confocal laser scanning microscope (CLSM).

2.13. The establishment of B16-F10 melanoma-bearing mouse models

This experiment used 5-week-old female C57BL/6J mice (certificate number 110324220104385532). 50 μL (2×10^5 cells) suspension of well-growing B16-F10 cells was subcutaneously inoculated into the right back of the mice, and the growth of the tumor was observed.

2.14. Intratumoral distribution

The tumor volume of the experimental mice was allowed to grow to around 80 mm^3. They were then randomly divided into 7 groups, namely the control group, the 1 h-1 patch group, the 1 h-2 patch group, the 3 h-1 patch group, the 3 h-2 patch group, the 6 h-1 patch group, and the 6 h-2 patch group, each group consisting of 4 mice. After the skin penetration of PVA/F-BPA microneedles, mice corresponding to each group were euthanized at 1 h, 3 h, and 6 h, respectively, and their relevant organs and tumor tissues were dissected and preserved. Finally, the boron concentration was determined by ICP-OES.

2.15. BNCT in B16-F10 melanoma-bearing mouse models

After the tumor volume of experimental mice reached around 80 mm^3, they were randomly divided into four groups: the PBS group, the PBS + N group, the PVA MNs + N group, and the PVA/F-BPA MNs + N group, with six mice in each group. After microneedle penetration and neutron irradiation (epithermal neutron flux: 3.37×10^7 n cm^{-2} s^{-1}, China Spallation Neutron Source, Dongguan), the survival status of the mice was observed, and the tumor volume was measured every two days.

The tumor size was measured using callipers, and the tumor volume (V) was calculated using the following equation: $V = a \times b^2/2$, where a and b are the major and minor axes, respectively.

2.16. Histological analysis for melanoma tumors

After 21 days, tumors and organs were collected and fixed with 4% paraformaldehyde. After dehydration, 5 μm thick paraffin sections were made and stained with HE. The tumor tissue was analyzed by immunofluorescence to observe DNA damage.

2.17. Immunofluorescence analysis of tumor tissues

After removing the paraffin from the tumor tissue sections and washing them with a gradient of ethanol, antigen retrieval was performed. The sections were washed three times with PBS for 5 minutes each time and then blocked with 2% BSA in a humid chamber at 37 °C for 30 minutes. After washing three times with PBS, the primary antibody was added and left to incubate overnight at 4 °C. The sections were then washed three times with PBS, and the secondary antibody was added and incubated at room temperature in the dark for 30 minutes. After washing three times with PBS (shaking during washing), the sections were mounted with glycerol buffer for microscopy examination.

2.18. Statistical analysis

All the obtained data were processed using GraphPad Prism v.8.0. The Student's t-test was used for two-group comparisons and multiple comparisons were evaluated using analysis of variance (ANOVA) models. The data were presented as the mean ± standard deviation (SD) of measurements (*$p < 0.05$, **$p < 0.01$, ***$p < 0.001$, and ****p < 0.0001). All the experiments were repeated at least three times.

3. Results and discussion

3.1. Characterization of microneedles

It is not easy to load BPA into dissolving MNs due to its poor water solubility. Therefore, instead of BPA, F-BPA, the structure and ^{1}H NMR results were shown in Fig. S1†, was synthesized and used to prepare dissolving MNs using a simple micromolding method. Microscopy images (Fig. 2a) and SEM results (Fig. 2b) showed that the PVA/F-BPA MNs were 8 mm × 8 mm

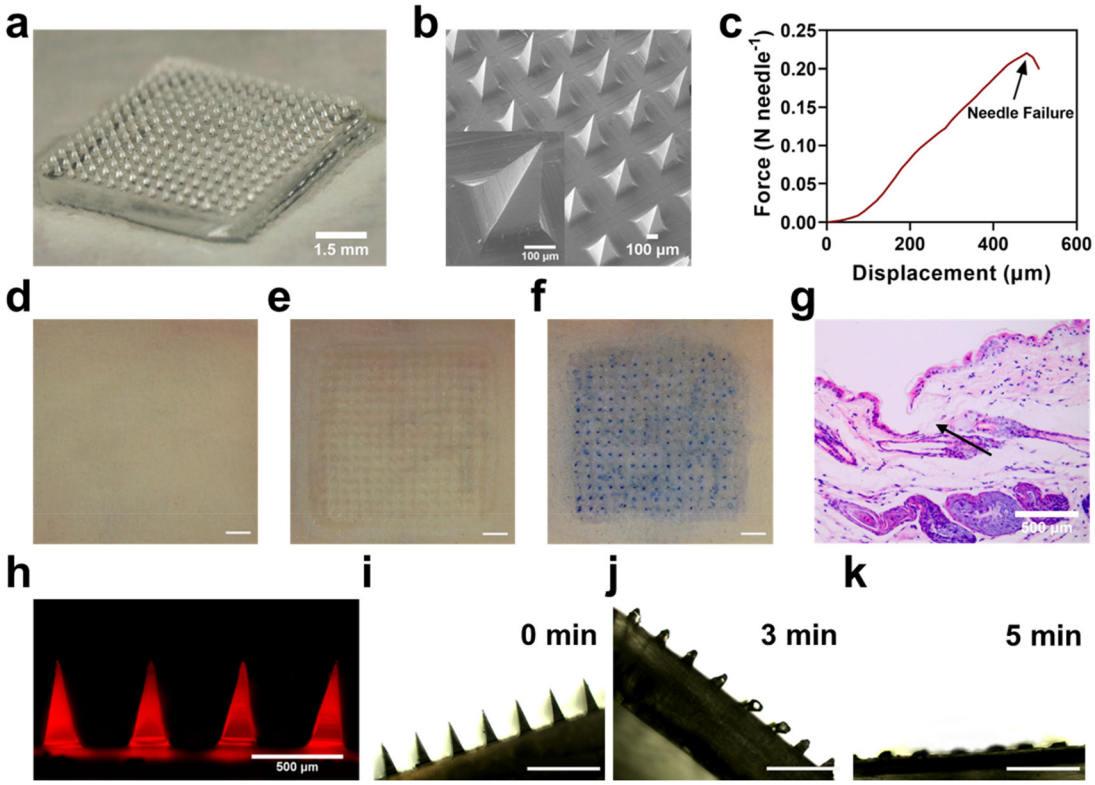

Fig. 2 Characterization of PVA/F-BPA MNs. (a) The overall morphology of PVA/F-BPA MNs. (b) SEM images of PVA/F-BPA MN arrays and tips. (c) Compression force *vs.* displacement plots of PVA/F-BPA MNs. (d and e) Images of mouse dorsal skin before and after pressing PVA/F-BPA MNs, scale bar: 1 mm. (f) Images of mouse dorsal skin after Taipan blue staining. Scale bar: 1 mm. (g) H&E stained section of skin after PVA/F-BPA MN penetration. Delicate punctures within the epidermis, resulting from the penetration of these microneedles, are clearly highlighted and elegantly indicated by a prominent arrow. (h) Fluorescence image of Cy5 labelled F-BPA distribution in the needle tips of PVA/F-BPA MNs ($\lambda_{excitation}$ = 650 nm). (i, j and k) Representative micrographs of PVA/F-BPA MNs before and 3 or 5 min after porcine skin insertion. Scale bar: 1000 μm.

in size, with the needle tips arranged in a 15 × 15 pyramidal shape and a 500 μm needle spacing. To facilitate the penetration of drugs into tumor lesions, microneedles should possess ample mechanical strength to pierce through the skin. Thus, the mechanical strength of the PVA/F-BPA MNs was measured and tested through compression experiments to assess the maximum pressure exerted on the microneedle tips. Fig. 2c shows that when the displacement reached 480 μm, the mean fracture force of needles of PVA/F-BPA MNs was 0.22 N, far higher than 0.058 N, the minimum force required to penetrate human skin.[25] Thus, PVA/F-BPA MNs maintained excellent insertion capability when applied to the skin. After MNs were pierced into the skin, the microneedle array was found to be consistent with the original microneedle array (Fig. 2d–g), which supported the fact that the microneedles were successfully and integrally pierced into the skin. To better show the distribution of F-BPA at the tip, Cy5-labelled F-BPA was synthesized using Cy5-fructose and BPA. Thus, PVA/Cy5-F-BPA microneedles were prepared and fluorescence images of the captured tips are shown in Fig. 2h, demonstrating that the drug was successfully and uniformly encapsulated in the tips. It was worth noting that a portion of Cy5-labelled F-BPA was also present in the PVA base of microneedles due to the diffusion of F-BPA (Fig. 2h). Meanwhile, the ^{10}B content in the microneedle tips of one patch of PVA/F-BPA MNs was found to be up to 9.10 μg by ICP-OES (Fig. S2†). Accumulation of ^{10}B in the needle tips could ensure that sufficient ^{10}B was delivered into the lesions. Furthermore, the dissolution characteristics of microneedles were also evaluated using porcine agarose gel. PVA/F-BPA MNs were found to dissolve after insertion into agarose until the needles completely disappear after 5 min (Fig. 2i–k and ESI Movie†), indicating the good dissolving ability of microneedles and the quick release of F-BPA.

The results revealed that PVA/F-BPA MNs displayed a consistently uniform and precisely defined morphological structure. Furthermore, they demonstrated commendable mechanical resilience, allowing them to effortlessly penetrate the skin. Subsequently, PVA/F-BPA MNs dissolved swiftly, ensuring the efficient delivery of a substantial ^{10}B payload deep into the layers of the skin.

3.2. Tumor cell uptake of ^{10}B

Cytotoxicity is a crucial index for evaluating the biocompatibility of biomaterials. Thus, different concentrations (from 0.003 ppm to 300 ppm) of F-BPA were added into B16-F10 cells, with PBS and PVA as controls, for a cell proliferation

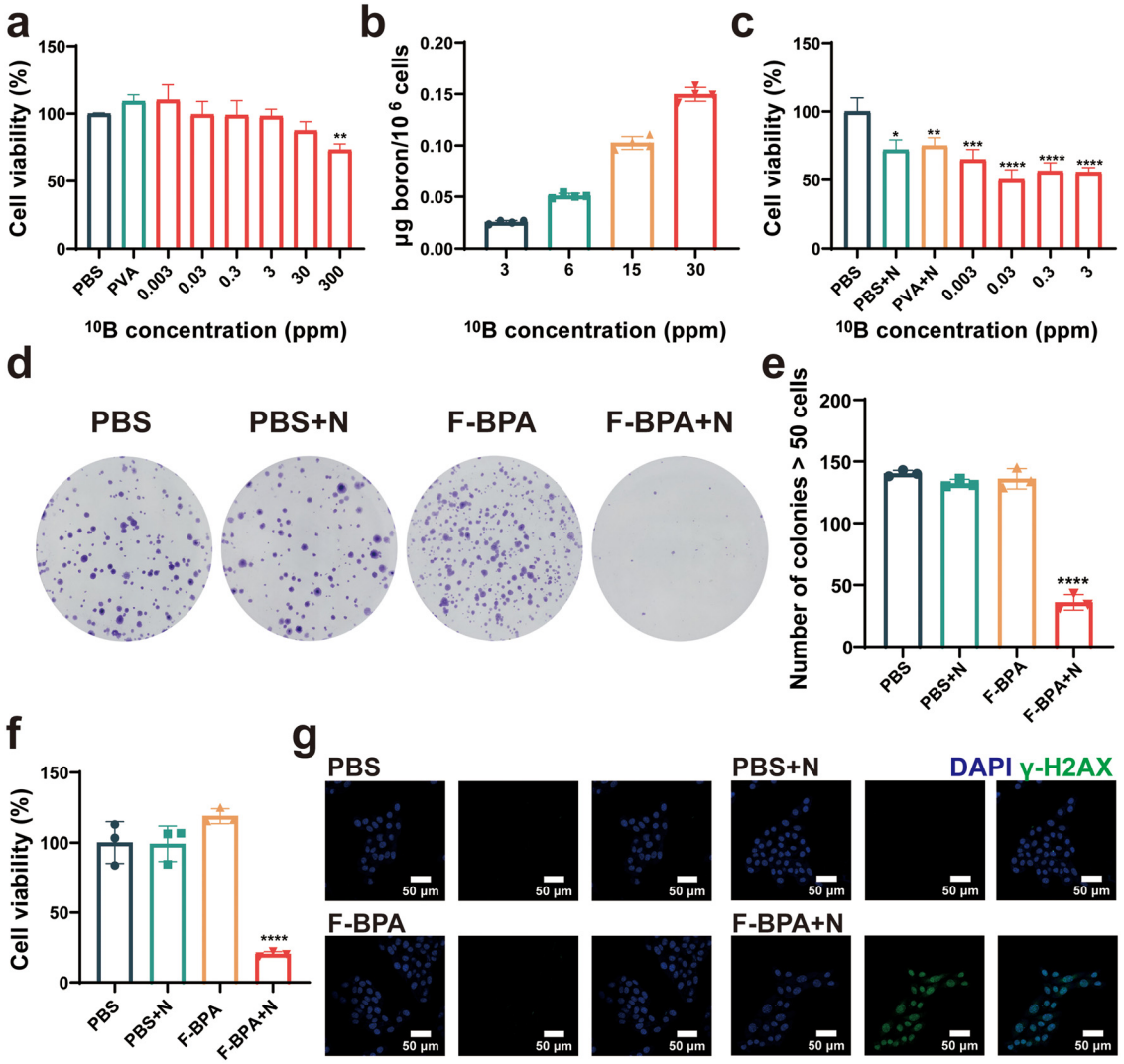

Fig. 3 Cell proliferation inhibition and DNA damage analysis. (a) The cytotoxicity of F-BPA at different concentrations measured by the CCK-8 assay. (b) Cellular uptake of F-BPA at different ^{10}B concentrations. (c) Toxic effects of neutron irradiation on cells measured by the CCK-8 assay. (d) Cell colony formation assay after F-BPA + N treatment and colonies were stained with crystal violet. (e) Quantification of the number of colonies consisting of at least 50 cells. (f) Measurement of cell viability after BNCT treatment by recording the absorbance (570 nm) of crystal violet stained with colonies. (g) Representative immunofluorescence images were recorded using confocal microscopy. Nuclei were stained with DAPI (blue) and an antibody to γ-H2AX (green). (*p < 0.05, **p < 0.01, ***p < 0.001,****p < 0.0001, compared with PBS group).

assay with a CCK-8 kit. As shown in Fig. 3a, the cells exhibited reduced activity only when cultured in a medium with a ^{10}B concentration of 300 ppm, which may be due to an increase in osmotic pressure inside and outside the cells followed by the increased fructose-BPA concentration. Once the concentration was lower than 300 ppm, the cells exhibited remarkable tolerance, thus demonstrating the material's excellent biocompatibility without toxicity to cells.

Additionally, efficient cell uptake is crucial for the BNCT-induced killing of cancer cells. Thus, it is essential to have a high and efficient cellular uptake of F-BPA for BNCT by using of PVA/F-BPA MNs. Based on previous reports,[5,6] LAT-1 is the transport protein of BPA and is overexpressed in tumors. The intracellular uptake of ^{10}B by cultured B16-F10 cells incubated with PVA/F-BPA for 3 h was from 21.7 ng per 10^6 cells to 0.123 μg per 10^6 cells as the ^{10}B concentration increased from 3 ppm to 30 ppm (Fig. 3b), which exceeded 16.67 ng per 10^6 cells as the critical concentration of ^{10}B for successful BNCT. Thus, PVA/F-BPA MNs were good candidates to deliver sufficient ^{10}B to B16-F10 cells by an efficient method.

3.3. The evaluation of BNCT efficacy *in vitro*

To determine the damaging effects of neutron irradiation on ^{10}B-containing cells, B16-F10 cells were incubated with PVA and F-BPA for 3 h and then subjected to neutron irradiation. The direct killing efficacy of B16-F10 cells cultured with different ^{10}B concentrations was evaluated using CCK-8 at 18 h after the neutron irradiation. The results indicated that

neutron irradiation could directly kill a small number of cells compared with the control samples without neutron irradiation (Fig. 3c). Compared with B16-F10 cells without ^{10}B, more B16-F10 cells with ^{10}B were directly killed, especially for B16-F10 cells at the ^{10}B concentration from 0.03 ppm to 3 ppm, resulting in lower cell viability. These results also demonstrated that BNCT efficacy was related to the ^{10}B concentration in the cells introduced above.

Previous research has reported that BNCT has the potential to damage DNA and presents significant obstacles to DNA repair mechanisms, affecting the ability of cell proliferation. Following neutron irradiation, tumor cells with damaged DNA were observed to remain viable, and their death was not immediate. Instead, these cells typically perished several days later due to an inability to repair their DNA. Therefore, we investigated cell proliferation post-irradiation by a cell colony assay which evaluated the capacity of individual cells to grow and expand into colonies. Following exposure to neutron irradiation, the colonies were permitted to thrive for a duration of five days. Subsequently, they underwent a treatment with a crystal violet stain, thereby enhancing their visual appeal and distinctiveness. As shown in Fig. 3d, it was pretty obvious that the number of colonies in the F-BPA + N (N means neutron irradiation) group was much less than that in the control groups. By further Image J analysis, the number of cell colonies in the F-BPA + N group was less than 50, while the number of cell colonies in the other groups was about 140, as shown in Fig. 3e. Besides, the OD value of the crystalline violet solution of each group was measured using a microplate reader, indicating the cellular activity of each group. As shown in Fig. 3f, the cellular activity of the F-BPA + N group was the lowest compared to the other groups.

To confirm DNA double-strand breaks induced by PVA/F-BPA MNs-BNCT, we conducted γ-H2AX staining on B16-F10 cells 8 hours post-neutron irradiation. This technique has proved to be a reliable method for quantifying unrepaired DNA double-strand breaks. The nucleus was labelled with DAPI and the γ-H2AX of the DNA double-strand break site could be detected and visualized by immunofluorescence labelling for analysis with confocal laser scanning microscopy techniques (CLSM). As shown in Fig. 3g, the green fluorescence in the nucleus region could be clearly observed in the F-BPA + N group compared with other groups, indicating that the cellular DNA in the F-BPA + N group was damaged. The above results demonstrated that combined fructose-BPA and neutron irradiation can cause cellular DNA damage.

In summary, the preceding discoveries indicated that PVA/F-BPA MNs-BNCT employed a dual-pronged strategy to impede the proliferation of B16-F10 cells. The initial approach involved the direct elimination of cells, albeit with constrained effectiveness. The secondary approach involved the induction of DNA damage, imposing substantial hurdles on DNA repair mechanisms and, consequently, impairing the cell's capacity to propagate. This latter mechanism emerged as the principal avenue through which PVA/F-BPA MNs-BNCT demonstrated its effectiveness.

3.4. Intratumoral distribution in B16-F10 melanoma-bearing mouse models

Successful BNCT relies on a high concentration of accumulated ^{10}B (>20 μg ^{10}B per g tumor tissue) in tumor cells and a high distribution ratio (T/N >3 : 1) of boron drug in tumor cells to normal cells to meet the requirement of neutron irradiation. To explore the potential of the transdermal drug delivery system of PVA/F-BPA MNs to effectively enhance the T/N ratio and deliver sufficient ^{10}B concentration at the tumor site, this experiment employed varying doses and dosing intervals. The ^{10}B concentration in the blood, organs and tumors of mouse models was measured by ICP-OES. The results presented in Fig. 4a indicated that three hours after the penetration of two patches of PVA/F-BPA MNs (in the 3 h-2 patch group), the concentration of ^{10}B in the tumor reached 23.12 μg per g tumor, which fulfilled the necessary criteria for BNCT therapy. In contrast, a single patch of PVA/F-BPA MNs was found to be insufficient for delivering adequate ^{10}B to melanoma. Besides, even with two patches of PVA/F-BPA MNs, one hour was deemed insufficient for tumor cells to take up sufficient F-BPA, and the concentration of ^{10}B at 6 hours was also below the desired level owing to the continuous efflux of intracellular F-BPA mediated by LAT-1. Thus, three hours after the penetration of two patches of PVA/F-BPA MNs was chosen as the starting time point of neutron irradiation for BNCT.

The T/N ratio plays a crucial role in BNCT as it aims to selectively target tumor cells while minimizing harm to the surrounding healthy tissues. A higher T/N ratio indicates greater therapy selectivity and improved chances of successful treatment outcomes. Nevertheless, achieving a high T/N ratio poses a significant challenge in the clinic. Using the transdermal drug delivery system of PVA/F-BPA MNs, we were surprised to find that the T/N ratio was greatly improved compared with previous reports on BNCT. For all treatment groups, the ^{10}B concentration in the blood was less than 0.1 μg ^{10}B per g blood (Fig. 4b), and the T/B (tumor/blood) ratio reached higher than 40 (Fig. 4c). In particular, the 3 h-2 patch group exhibited an extremely high T/B ratio of 252.46 (Fig. 4c), which was chosen as the optimum experimental condition for further treatment in B16-F10 melanoma-bearing mouse models. Moreover, for the organs like the heart, liver, spleen, lungs, and kidneys, the T/N ratios in the 3 h-2 patch group ranged from 93.16 to 162.71 (Fig. 4e). The low accumulation of ^{10}B in blood and other organs and super-high T/N ratios were also observed in other experimental groups after the transdermal drug delivery system of PVA/F-BPA MNs (Fig. 4d, e and S3†).

All these results indicated that the transdermal drug delivery system of PVA/F-BPA MNs could efficiently deliver sufficient F-BPA to melanoma after the penetration of 2 patches. More importantly, it was confirmed that the transdermal drug delivery system of PVA/F-BPA MNs could significantly improve the T/N ratio, reducing the accumulation of ^{10}B in blood and other organs, compared with the traditional intravenous injection method.

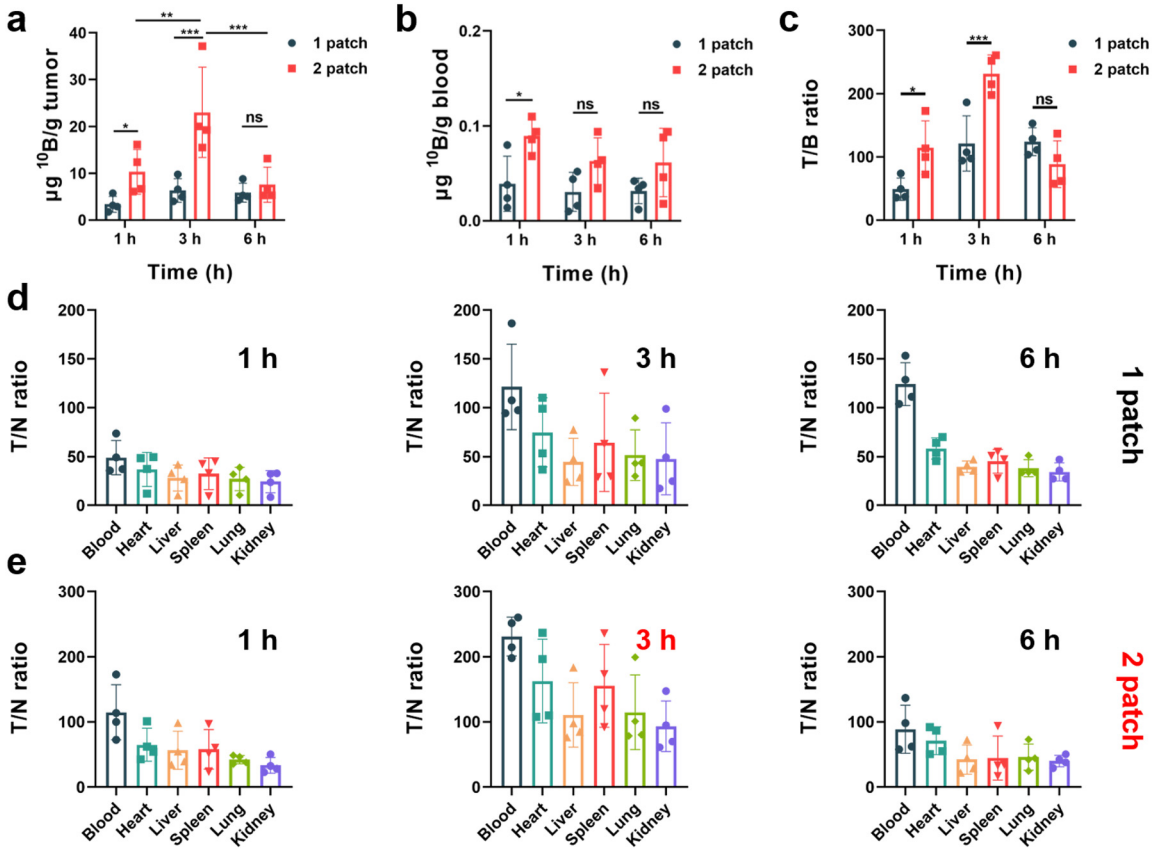

Fig. 4 Intratumoral distribution in B16-F10 melanoma-bearing mouse models after treatment with the transdermal drug delivery system of PVA/F-BPA MNs. The ^{10}B concentration (n = 4) in tumor tissue (a) and blood (b) measured by ICP-OES at different times after the penetration of one or two patches of PVA/F-BPA MNs. (c) Tumor-to-blood ratios (T/B ratios) of mouse models at different times after the penetration of one or two patches of PVA/F-BPA MNs. The T/N ratios (n = 4) (including blood, the heart, liver, spleen, lungs and kidneys) of mouse models at different times after the penetration of one (d) or two (e) patches of PVA/F-BPA MNs. (*P < 0.05, **P < 0.01, ***p < 0.001, ns > 0.05).

3.5. PVA/F-BPA MNs for BNCT *in vivo*

To detect the *in vivo* anti-tumor effect of the transdermal drug delivery system of PVA/F-BPA MNs, B16-F10 melanoma-bearing mice were divided into four groups including PBS, PBS + N, PVA MNs + N, and PVA/F-BPA MNs + N groups (N means neutron irradiation) and then subjected to neutron irradiation (except the PBS group) 3 hours after the penetration of two patches of microneedles or injection of PBS. Then the mice were sacrificed on day 21 (Fig. 5a). In the irradiation procedure, the mice were thoughtfully placed in a specially crafted circular setup after being gently anesthetized, guaranteeing their uniform distribution, with their tumors precisely aligned towards the central point of the neutron beam. This meticulous arrangement allowed for precise targeting of the tumors, exposing them to thermal neutrons while ensuring that the neighboring organs such as the liver, spleen, and intestines were effectively shielded from radiation. This precautionary measure was taken to minimize the potential for any harm or damage to these vital organs.

Tumor volumes were measured routinely to assess the treatment effectiveness of BNCT. Once the tumor volume reached 2000 mm^3, the corresponding mice were regarded as dead and sacrificed. For the groups of PBS, PBS + N, and PVA MNs + N, all experimental mice (n = 6) were dead on days 12, 16 and 14, respectively (Fig. 5c and S4†). In contrast, upon treatment with PVA MNs + N, remarkable suppressions of tumor growth were observed. For the PVA MNs + N group, the tumor volume reached 539.1 mm^3, with an increase of approximately 8.16-fold (Fig. 5b), and the survival time of mice was prolonged to 21 days for 4 mice among the group (Fig. 5c and S4†). Thus, the results of tumor growth and mouse survival indicated that the treatment combining the transdermal drug delivery system of PVA/F-BPA MNs with thermal neutron irradiation specifically suppressed the growth of tumors.

In order to further confirm the suppression of tumor in the PVA MNs + N group, H&E staining experiments and immunofluorescence analysis were conducted. The histopathological analysis shown in Fig. 5e revealed that the tumor cells in the PVA/F-BPA MNs + N group exhibited extensive necrosis, while the cells in the remaining three groups maintained a healthy state. These findings strongly indicated a potent killing effect of PVA/F-BPA MNs-BNCT. In addition, γ-H2AX is regarded as a marker of DNA double-strand breaks induced by radiotherapy.

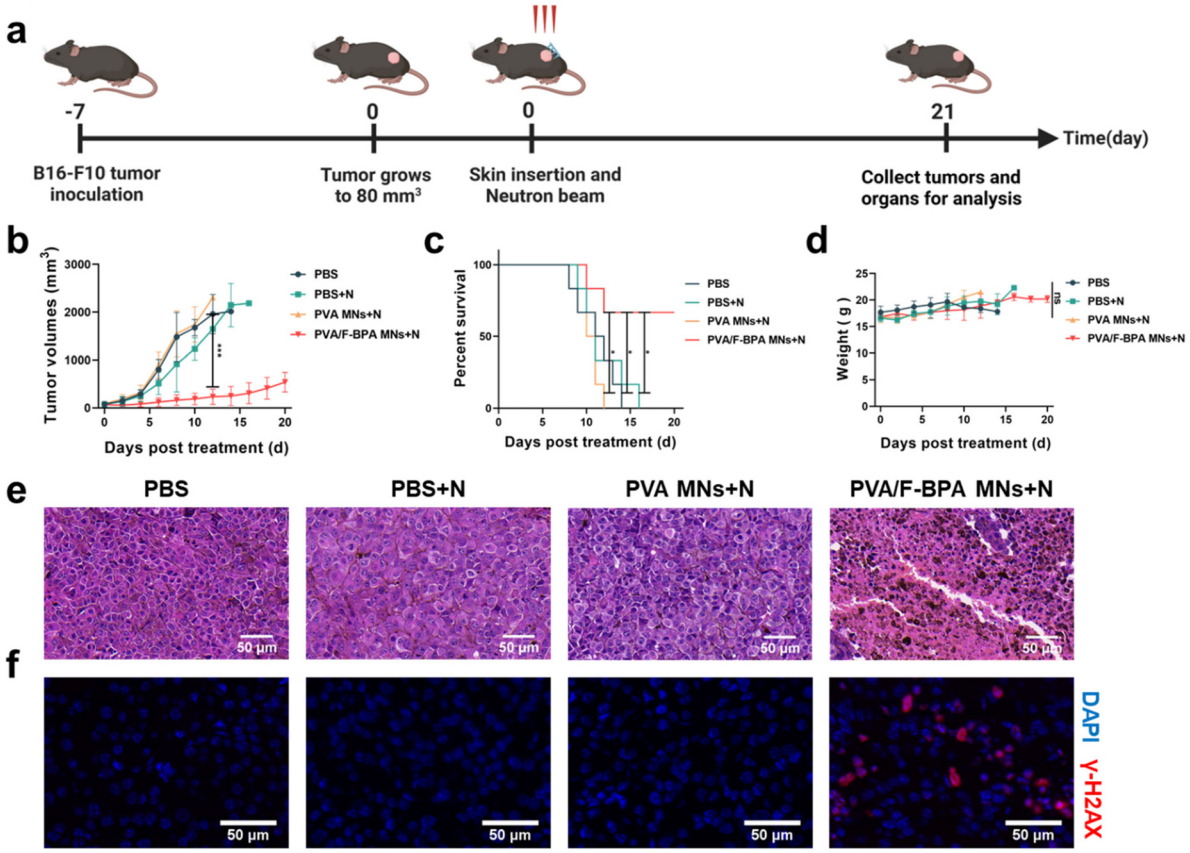

Fig. 5 The inhibitory effect of PVA/F-BPA MNs-BNCT on tumor growth *in vivo*. (a) Scheme of the experimental timeline. (b) Body weight curve of the individual mouse at indicated time points after BNCT experiments. (n = 6, ***p < 0.001). (c) Tumor growth curves. (n = 6, *P < 0.05). (d) Survival curves of mice after various treatments as indicated (0–21 days). (n = 6, ns > 0.05). (e) H&E staining of tumor tissues collected 21 days after the indicated treatments. (f) Representative tumor tissues' immunofluorescence images were recorded using confocal microscopy. Nuclei were stained with DAPI (blue) and antibodies to γH2AX (red).

To confirm the DNA double-strand breaks by BNCT, immunofluorescence analysis of γ-H2AX was performed, and the γ-H2AX signal intensity (red fluorescence) was found to be significantly higher than that in other groups (Fig. 5f). These results were consistent with the H&E staining analysis and also proved the conclusion we drew from the immunofluorescence analysis of γ-H2AX *in vitro* that damaging DNA double-strand breaks appeared to be the primary mechanism of tumor suppression for BNCT. This further illustrated that PVA/F-BPA MNs combined with BNCT can significantly inhibit tumor growth.

Moreover, as shown in Fig. 5d, there was no significant difference in the change of the body weight of mice in all groups during the treatment period, and no tissue damage was observed in major organs (heart, liver, spleen, lungs and kidneys) according to the histological analysis (Fig. S5†). Thus, no radiation or biochemical toxicity to normal tissues was observed, owing to the extremely high T/N ratio for the transdermal drug delivery system and the limited irradiation area outside of the normal organs. Thus, these results demonstrated that combining the transdermal drug delivery system of PVA/F-BPA MNs and BNCT represented a powerful antitumor strategy with good biological safety.

4. Conclusions

In this work, we designed PVA microneedles loaded with F-BPA as the transdermal drug delivery system for BNCT. The morphology and mechanical strength of the microneedles demonstrated that PVA/F-BPA MNs had a complete microneedle array and skin insertion ability. The microneedles showed great dissolving ability and the needles could completely disappear within 5 min after penetration. Besides, PVA/F-BPA MNs showed good biocompatibility, as confirmed by the CCK-8 assay, and sufficient cellular uptake of F-BPA was confirmed by the ICP-OES data. Fluorescent labelling of the γ-H2AX antibody and cell proliferation experiments demonstrated the effect of DNA damage on cell proliferation for BNCT *in vitro*. Besides, the *in vivo* distribution analysis of tumor-bearing mice showed that the transdermal drug delivery system of PVA/F-BPA MNs could efficiently deliver sufficient F-BPA to melanoma after administration with 2 patches. Remarkably, this system substantially improved the T/N ratio, surpassing 93.16, thereby reducing the accumulation of ^{10}B in blood and other organs. This represented a significant advantage over traditional intravenous injection methods. Finally, the treatment combining

PVA/F-BPA MNs and neutron irradiation could significantly inhibit tumor growth and improve mice's survival rates. Therefore, this dissolving microneedle-based transdermal drug delivery system not only simplified the preparation and treatment procedures for BNCT but also demonstrated potent therapeutic effects for melanoma. Particularly, the exceptionally high T/N ratio positions microneedles-BNCT as a promising approach for future clinical tumor treatments.

Author contributions

J. L., X. W., H. L. and Z. L. designed and discussed the experiments, while J. L. carried out most experiments, supported by analytical/experimental contributions by X. W., Z. W., Z. Z., Y. Z., L. L., D. D., J. G., and J. Z. The manuscript draft was written by J. L. and X. W. with the review and editing by H. L. and Z. L. All authors have given approval to the final version of the manuscript.

Conflicts of interest

There are no conflicts to declare.

Acknowledgements

This work was supported by the Guangdong Basic and Applied Basic Research Foundation (2021B1515120065), the National Natural Science Foundation of China (82202339, 82202307 and 22207050), the China Postdoctoral Science Foundation (2022M711527 and 2021M701640), the Priority Strategy Project of the Key Laboratory of Medicinal Chemistry and Molecular Diagnosis of the Ministry of Education (No. ts2020004), and the National High-End Foreign Expert Recruitment Plan (G2022003007L).

The authors thank Prof. Jianfei Tong, Lingbo Zhu and Shengqiang Wei from the China Spallation Neutron Source (CSNS) for their assistance with BNCT experiments.

References

1 R. F. Barth and A. H. Soloway, *J. Neuro-Oncol.*, 1997, **33**, 3–7.
2 R. L. Moss, *Appl. Radiat. Isot.*, 2014, **88**, 2–11.
3 Q. Dai, Q. Yang, X. Bao, J. Chen, M. Han and Q. Wei, *Mol. Pharm.*, 2022, **19**, 363–377.
4 M. Lamba, A. Goswami and A. Bandyopadhyay, *Chem. Commun.*, 2021, **57**, 827–839.
5 T. Nomoto, Y. Inoue, Y. Yao, M. Suzuki, K. Kanamori, H. Takemoto, M. Matsui, K. Tomoda and N. Nishiyama, *Sci. Adv.*, 2020, **6**, eaaz1722.
6 T. Nomoto, Y. Yao, Y. Inoue, M. Suzuki, K. Kanamori, H. Takemoto, M. Matsui, K. Tomoda and N. Nishiyama, *J. Controlled Release*, 2021, **332**, 184–193.
7 Y. Mori, A. Suzuki, K. Yoshino and H. Kakihana, *Pigm. Cell Res.*, 1989, **2**, 273–277.
8 R. F. Barth, J. A. Coderre, M. G. Vicente and T. E. Blue, *Clin. Cancer Res.*, 2005, **11**, 3987–4002.
9 H. Fukuda, C. Honda, N. Wadabayashi, T. Kobayashi, K. Yoshino, J. Hiratsuka, J. Takahashi, T. Akaizawa, Y. Abe, M. Ichihashi and Y. Mishima, *Melanoma Res.*, 1999, **9**, 75–83.
10 R. F. Barth, P. Mi and W. Yang, *Cancer Commun.*, 2018, **38**, 35.
11 J. Li, J. Kong, S. Ma, J. Li, M. Mao, K. Chen, Z. Chen, J. Zhang, Y. Chang, H. Yuan, T. Liu, Z. Zhang and G. Xing, *Adv. Funct. Mater.*, 2021, **31**, 2100969.
12 V. Torresan, A. Guadagnini, D. Badocco, P. Pastore, G. A. Munoz Medina, M. B. Fernandez van Raap, I. Postuma, S. Bortolussi, M. Bekic, M. Colic, M. Gerosa, A. Busato, P. Marzola and V. Amendola, *Adv. Healthc. Mater.*, 2021, **10**, e2001632.
13 N. Kuthala, R. Vankayala, Y. N. Li, C. S. Chiang and K. C. Hwang, *Adv. Mater.*, 2017, **29**, 1700850.
14 N. Kuthala, M. Shanmugam, C. L. Yao, C. S. Chiang and K. C. Hwang, *Biomaterials*, 2022, **290**, 121861.
15 L. Dai, J. Liu, X. Zhao, Y. Li, S. Zhou, L. Yuan, D. Shu, L. Pan, Y. h. Liu and Z. Qian, *Adv. Funct. Mater.*, 2023, 2214145.
16 A. Kim, M. Suzuki, Y. Matsumoto, N. Fukumitsu and Y. Nagasaki, *Biomaterials*, 2021, **268**, 120551.
17 J. Li, Q. Sun, C. Lu, H. Xiao, Z. Guo, D. Duan, Z. Zhang, T. Liu and Z. Liu, *Nat. Commun.*, 2022, **13**, 2143.
18 Z. Wang, Z. Yang, J. Jiang, Z. Shi, Y. Mao, N. Qin and T. H. Tao, *Adv. Mater.*, 2022, **34**, e2106606.
19 J. Yu, Y. Zhang, Y. Ye, R. DiSanto, W. Sun, D. Ranson, F. S. Ligler, J. B. Buse and Z. Gu, *Proc. Natl. Acad. Sci. U. S. A.*, 2015, **112**, 8260–8265.
20 J. Yu, J. Wang, Y. Zhang, G. Chen, W. Mao, Y. Ye, A. R. Kahkoska, J. B. Buse, R. Langer and Z. Gu, *Nat. Biomed. Eng.*, 2020, **4**, 499–506.
21 K. J. Koh, Y. Liu, S. H. Lim, X. J. Loh, L. Kang, C. Y. Lim and K. K. L. Phua, *Sci. Rep.*, 2018, **8**, 11842.
22 N. W. Kim, S. Y. Kim, J. E. Lee, Y. Yin, J. H. Lee, S. Y. Lim, E. S. Kim, H. T. T. Duong, H. K. Kim, S. Kim, J. E. Kim, D. S. Lee, J. Kim, M. S. Lee, Y. T. Lim and J. H. Jeong, *ACS Nano*, 2018, **12**, 9702–9713.
23 C. Wang, Y. Ye, G. M. Hochu, H. Sadeghifar and Z. Gu, *Nano Lett.*, 2016, **16**, 2334–2340.
24 E. Zhao, T. Xiao, Y. Tan, X. Zhou, Y. Li, X. Wang, K. Zhang, C. Ou, J. Zhang, Z. Li and H. Liu, *ACS Appl. Mater. Interfaces*, 2023, **15**, 7725–7734.
25 Q. Bian, L. Huang, Y. Xu, R. Wang, Y. Gu, A. Yuan, X. Ma, J. Hu, Y. Rao, D. Xu, H. Wang and J. Gao, *ACS Nano*, 2021, **15**, 19468–19479.
26 Y. Li, G. He, L. H. Fu, M. R. Younis, T. He, Y. Chen, J. Lin, Z. Li and P. Huang, *ACS Nano*, 2022, **16**, 17298–17312.
27 X. Xue, H. Qu and Y. Li, *Exploration*, 2022, **2**, 20210134.
28 Y. Zhang, Y. Xu, H. Kong, J. Zhang, H. F. Chan, J. Wang, D. Shao, Y. Tao and M. Li, *Exploration*, 2023, **3**, 20210170.

29 M. C. Chen, Z. W. Lin and M. H. Ling, *ACS Nano*, 2016, **10**, 93–101.
30 S. Khan, A. Hasan, F. Attar, M. M. N. Babadaei, H. A. Zeinabad, M. Salehi, M. Alizadeh, M. Hassan, H. Derakhshankhah, M. R. Hamblin, Q. Bai, M. Sharifi, M. Falahati and T. L. M. Ten Hagen, *J. Controlled Release*, 2021, **338**, 341–357.
31 J. Chen, Z. Jiang, Y. S. Zhang, J. Ding and X. Chen, *Appl. Phys. Rev.*, 2021, **8**, 041321.
32 H. P. Tham, K. Xu, W. Q. Lim, H. Chen, M. Zheng, T. G. S. Thng, S. S. Venkatraman, C. Xu and Y. Zhao, *ACS Nano*, 2018, **12**, 11936–11948.
33 M. Chen, D. Yang, Y. Sun, T. Liu, W. Wang, J. Fu, Q. Wang, X. Bai, G. Quan, X. Pan and C. Wu, *ACS Nano*, 2021, **15**, 3387–3401.
34 G. Yang, Y. Liu, J. Chen, J. Ding and X. Chen, *Acc. Mater. Res.*, 2022, **3**, 1232–1247.